American Mineralogist, Volume 85, pages 1784–1794, 2000

Charge contrast imaging of geological materials in the environmental scanning electron microscope

GORDON R. WATT,[1,*,†] BRENDAN J. GRIFFIN,[2] AND PETER D. KINNY[1]

[1]Tectonics Special Research Centre, School of Applied Geology, Curtin University of Technology, GPO Box U1987, Perth 6845, Western Australia, Australia

[2]Centre for Microscopy and Microanalysis, The University of Western Australia, Nedlands, Western Australia, 6907, Australia

ABSTRACT

The environmental scanning electron microscope (ESEM) allows high-resolution, high-magnification imaging of conductivity differences in uncoated geological samples. Under normal ESEM operating conditions, negative charge buildup at the sample surface (from bombardment by the electron beam) is prevented by the presence of a gas (usually water vapor) in the sample chamber. Backscattered and secondary electrons from the sample ionize this chamber gas, and the resultant positively charged gaseous ions migrate toward the negatively charged sample. When chamber gas pressures lower than approximately 250 Pa are used, however, charging of the sample can occur because insufficient charge balancing positively charged gaseous ions are produced. Charge implantation in the sample alters secondary electron emission, and, because intracrystalline conductivity contrasts occur in response to variations in defect density, secondary electron images reflect compositional variations and/or microstructural features. These secondary electron images are referred to as charge contrast images (CCI). To demonstrate potential geological applications of CCI, we present images of growth zones, microfractures, differential diffusion domains, pleochroic haloes, and relict fluid pathways from zircon (strongly luminescent), quartz (weakly luminescent), and biotite and cordierite (non-luminescent). CCI detect defects in a similar way to cathodoluminescence (CL), but have a higher resolution because the CCI signal is composed of secondary electrons that are generated from a much smaller interaction volume than photons utilized in CL. CCI imaging also can be applied to a wider variety of geological samples than CL, because electronic charge trapping is not restricted to wide-band gap electronic configurations. One of the most important potential applications of the CCI technique may lie in the direct imaging of relict fluid pathways in rocks that have experienced metasomatism or alteration.

INTRODUCTION

Electron microscopy has several advantages over conventional light microscopy, most notably better spatial resolution and greater depth of field (Lloyd and Hall 1981; Trimby and Prior 1999), and high-resolution topographic, structural, and compositional images from scanning electron microscopes are now widely used in the earth sciences. The principle of scanning electron microscopy is simple—electrons from a thermionic or field-emission cathode are accelerated to form a beam that is rastered across the sample surface. Signals arising from interactions between the beam and sample are collected, and an image reconstructed that reflects variations in signal strength. The bombardment of geological materials with a beam of electrons, however, will generally result in electrical charging and specimen damage unless steps are taken to reduce charge buildup. The most common method used to alleviate sample charging involves coating the specimen surface with a thin (50 nm) conductive layer of C, Au, or Pt. Conductive coats can reduce signal/noise, compromise weak or low-energy signals, and/or obscure important emissions (e.g., Au$M\alpha$ X-ray emission from a gold coat may conceal Nb$L\alpha$ signals in niobates). A conductive coat also prevents the direct imaging of conductivity contrasts in the underlying substrate. In uncoated samples, differences in the dielectric properties generate charge contrasts that may be used to detect compositional variations, structural contrasts, and enhanced conductivity pathways within and between minerals. Despite an abundance of materials science literature linking electron trapping and charging in semiconductors and ceramics with defects of geological significance (e.g., trace element impurities, lattice defects, twin planes) (Doehne 1998; Galvin and Griffin 1999; Gluszak et al. 1999; Gong et al. 1993; Oh et al. 1993), little attention has been paid to the phenomenon of charge contrast in geological samples.

In this paper, we show that charging contrasts within single crystals and among mineral phases can provide important information regarding growth, compositional variation, microstructure, and alteration in a variety of geological specimens. We image several minerals and compare the information from charge contrast with other electron imaging techniques such as backscattered electron (BSE) imaging and cathodoluminescence (CL). The samples presented include cathodoluminescent phases (zircon and quartz) and non-lumi-

* E-mail: gordon@lithos.fsnet.co.uk

† Current Address: Department of Geology & Petroleum Geology, King's College, University of Aberdeen, Aberdeen, AB24 3UE, U.K.

nescent phases (cordierite and biotite). These minerals were chosen to illustrate various intra- and inter-grain charge contrast features and demonstrate potential applications for charge-contrast imaging—a new high-resolution, non-destructive petrographic tool for earth scientists.

ENVIRONMENTAL SCANNING ELECTRON MICROSCOPY

The environmental scanning electron microscope (ESEM) allows the observation of uncoated samples at moderate to low vacuums (Danilatos 1993; Griffin 1997a). In the ESEM, the primary electron beam and backscattered and secondary electrons from the sample interact with gas molecules in the specimen chamber to produce positively charged gaseous ions and an amplified "cascade" of secondary electrons that are accelerated toward a positively biased gaseous secondary electron detector (GSED) (Danilatos 1993). Once the gas is ionized, it migrates toward the sample where it acts as a charge-neutralizing agent. The ESEM is normally operated at high enough gas pressures to produce sufficient positive gaseous ions to neutralize charge at the sample surface and, consequently, most ESEM images show no charging. At lower gas pressures, however, it is possible to implant a limited amount of charge in an uncoated sample (Doehne 1998; Griffin 1997). These implanted electrons modify secondary electron emission from the sample surface and produce contrast between areas of different conductivity, allowing the direct imaging of subtle compositional variations and microstructural features (Griffin 1997, 1998).

A schematic diagram of a typical ESEM is shown in Figure 1. The principal difference between an ESEM and conventional SEM lies in the differential pumping system in the column, which allows a series of pressure stages between the specimen chamber (held at a low vacuum of between 0 and 3000 Pa) and the gun (10^{-5} Pa) (Danilatos 1993). The pressure of the specimen chamber is adjustable, and a variety of gases may be introduced depending on the sample and processes to be observed. The ESEM can be likened to a parallel-plate gas capacitor (Meredith et al. 1996), with the chamber gas acting as an amplifying medium to facilitate detection of secondary electrons emitted from the sample. The degree of gas amplification is dependent on ionization potential of the chamber gas and the gas pressure in the chamber, with most gases reaching a maximum total amplification at around 150–1500 Pa (Thiel et al. 1997). Water vapor is the most commonly used chamber gas, as it has a relatively low ionization potential (producing maximum signal amplification) and a high charge neutralization capacity. Inert gases such as Ar and He produce much less gas amplification at room temperature than H_2O, but ionize more readily at higher temperatures (Meredith et al. 1996).

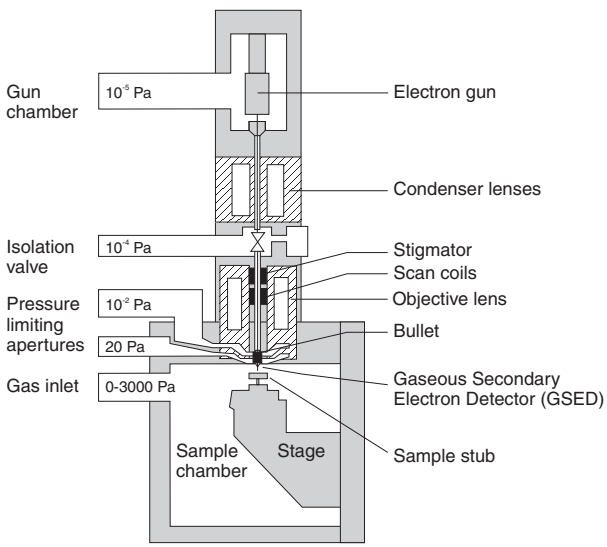

FIGURE 1. Schematic cross section of an Electroscan ESEM3 (after Danilatos 1993). The instrument consists of a column and a chamber. A stepped series of vacuum stages allows the electron gun (top) to be held at a high vacuum while the sample chamber operates at a range of gas pressures.

Secondary electron images in the ESEM are generated from the signal collected at the positively biased GSED (Meredith 1996). The signal received at the GSED is composed of a "cascade" of secondary electrons derived from several sources (Fig. 2). These include the following. (1) Secondary electrons generated by the primary beam at the sample surface (SE1). (2) Secondary electrons generated at the sample surface by exiting backscattered electrons or during ionizing collisions between backscattered electrons and the chamber gas (SE2). (3) Secondary electrons generated by backscattered electrons colliding with the GSED (SE3). (4) Secondary electrons derived from ionizing collisions between the primary beam and the chamber gas (SE4).

Additional secondary electrons are generated during collisions between ionized gas molecules and the sample surface and between individual ionized gas molecules (Thumm et al. 1999). Meredith et al. (1996) demonstrated that in materials with low mean atomic numbers (e.g., graphite), the total amplified electron signal is dominated by SE1 secondary electrons, whereas SE2 + SE3 + SE4 electrons comprise less than 10% of the total signal. In contrast, typical geological materials have relatively high mean atomic numbers (backscattered electron coefficients), and SE2 + SE3 electrons comprise a larger part of the total signal received at the GSED.

CHARGE-CONTRAST IMAGING

Several workers have reported "anomalous" contrast when working at low gas pressures in the ESEM, or when examining uncoated specimens at low voltages in conventional SEMs (Doehne 1998), which they have ascribed to charging. The earliest report of charge contrast was from uncoated SiC, a reaction-bonded ceramic, in a conventional SEM (Sawyer and Page 1978). These authors ascribed a strong secondary electron emission contrast between pre-existing cores and newly crystallized reaction rims to the distribution of trace-element impurities and suggested that the presence of these trace elements generated defects that altered the escape probability of secondary electrons. Charge-contrast imaging studies of materials of geological interest involved imaging of growth structure of uncoated diamond in a conventional SEM (Harker et al. 1993, 1994). Differential charge dissipation along twin planes and

highly connected pathways between twin planes and grain-boundaries was noted. Several subsequent ESEM studies have demonstrated CCI as an effective imaging technique for various minerals including calcite (Doehne 1998), zircon (Griffin 1998), gibbsite (Baroni et al. 1999; Griffin 1997), sphalerite (Griffin 1998), quartz (Newton-Howes et al. 1989), and fused silica (Galvin and Griffin 1999).

The exact origin of the charge contrast signal is poorly understood, but a general model invokes modified secondary electron emission at the sample surface resulting from charge implantation. When an uncoated, ungrounded specimen is bombarded by electrons it will become negatively charged if the number of secondary and backscattered electrons emitted is smaller than the number of electrons incident on the sample (Reimer 1985). Under normal operating conditions in the electron microscope, this situation occurs at beam energies above 3–4 keV. During irradiation, electron-hole pairs form. Most of these pairs recombine, but a few electrons may move in conductance and valence bands before being trapped (Vigouroux et al. 1985). Although experiments have shown that dissipation (detrapping) of implanted charge occurs nearly instantaneously (Kronenberg and Kirby 1987), most studies suggest that charge build-up in wide-band gap insulators such as silica occurs due to localization of electrons at defects (Griscom 1990; Siegel and Marrone 1981). Defects may be induced by irradiation (extrinsic defects) or, more commonly, exist in the specimen prior to bombardment by electrons (intrinsic defects). Typical charge-trapping intrinsic defects in silicates include strained-bond regions around trace elements, dangling bonds, non-bridging O atoms, E' centers (an unpaired electron in a dangling tetrahedral sp^3 orbital of an Si atom bonded to three oxygen atoms (Stevens Kalceff and Phillips 1995), and peroxyl (OH) linkages (Griscom 1990; Stevens Kalceff and Phillips 1995; Stevens Kalceff et al. 1999).

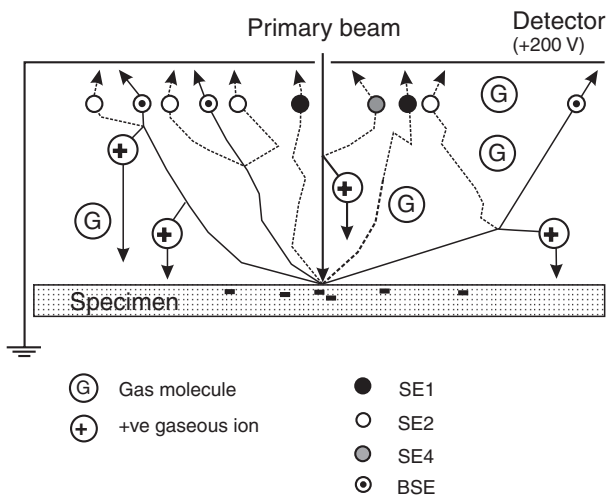

FIGURE 2. A schematic diagram showing the origin of signals generated in the ESEM chamber. SE1 electrons are low-energy secondary electrons generated at the sample surface by elastic collisions with the beam. They are accelerated to the detector by a small positive bias. SE2 electrons form by ionizing collisions between backscattered electrons (BSE) and chamber gases, and are termed "cascade" electrons. A small component of SE4 electrons arise from collisions between primary beam electrons and the chamber gas. Positive ions produced by the formation of SE2 are attracted to the negatively charged sample in an ion flood.

The distribution of trapped charge in electron-irradiated quartz has been shown to be directly related to the defect density and temperature (Oh et al. 1993), leading some authors to suggest that charge contrast results from the enhancement of SE1 secondary electron emission above implanted charge (Doehne 1998). In an alternative model, Griffin (1998) proposed that suppression of SE1 emission at the sample surface occurs due to the presence of positive ions from ionized chamber gas. Because of the "cascade" effect, gas ionization may actually result in positive ion currents at the sample surface up to two orders of magnitude greater than the incident electron beam current. At high gas pressures, therefore, charging effects are minimized and SE1 electron emission suppressed, leading to SE2 dominated images. At lower gas pressures and under certain conditions in conventional SEMs, however, the effects of charge buildup on SE1 emission are retained and charge-contrast images are produced (Fig. 3).

METHODS

Charge-contrast images are stable once obtained, but sensitive to working conditions (including accelerating voltage, scan rate, chamber gas pressure, and working distance). Small changes in operating conditions may dramatically alter the sensitive balance between positive ion flood and electron emission and cause contrast reversal under certain conditions (Griffin 1998). Contrast reversal has been observed by Doehne (1998), who suggested that higher charge contrast is obtained at faster scan rates because electron detrapping between scans is minimized and more charge build-up can occur.

High accelerating voltages produce the strongest charge contrast, but contrast resulting from charge implantation has been observed at accelerating voltages as low as 5 kV (Griffin 1997). Whereas high accelerating voltages produce the strongest SE1 + SE2 electron emission and strongest contrast, an inverse relationship between signal strength and spatial resolution means that accelerating voltages around 30 kV are typically used. Chamber pressure and working distance strongly influence the balance between the emission of secondary electrons to produce a signal and signal suppression by the positive ion flood at the sample surface (Griffin 1997). As noted above, at high gas pressures, the positive ion flood at the sample surface suppresses SE1 emission, and images appear "flat" because the signal is dominated by SE2 produced by backscattered electrons that have their source deeper in the sample. At lower gas pressures, the positive ion flood is smaller, and a higher proportion of SE1 electrons can escape from the sample. In our experience, the best charge-contrast images are usually obtained at gas pressures of 2.0 Torr (250 Pa) or less, using water vapor as a chamber gas. The actual pressure depends on the beam dosage, the mineral phase (or phases) being analyzed, working distance, and the sensitivity of the GSED.

The charge-contrast images presented here were collected on an Electroscan E3 ESEM equipped with LINK Si(Li) EDS, BSE, and CL detectors, and a Philips XL40 ESEM fitted with

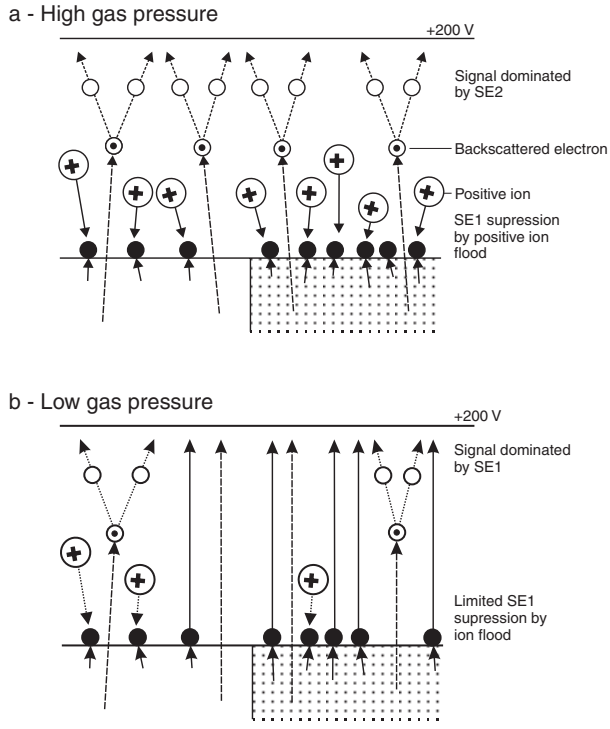

FIGURE 3. (**a**) Schematic diagram showing processes occurring at high gas pressures. The sample consists of two regions with different defect densities (open circles)—a defect-poor region (left) and a region rich in defects (stippled, right). All other symbols as in Figure 2. No difference in SE1 emission between the two areas occurs at high gas pressures because SE1 emission is suppressed by a high positive ion flux. The detected signal is thus dominated by SE2 electrons formed by ionizing collisions. (**b**) In contrast, at lower gas pressures, there is only limited supression of SE1 by the positive ion flood and the resulting signal is dominated by SE1. Because SE1 generation is enhanced by defects, the defect-rich region generates a brighter signal.

BSE, an Oxford Instruments OPAL fore-scattered electron detector, and a MiniCL detector. Both instruments are housed at the Centre for Microscopy and Microanalysis, University of Western Australia. Cathodoluminescence images were collected on a Philips XL40 and a JEOL JSM–6400R at UWA, and a Phillips XL30 SEM at Curtin University. ESEM backscattered electron images were collected using a 0 V gain on the GSED, because gas luminescence in the ESEM chamber may generate a spurious signal at the light-sensitive BSE detector. All samples were normally polished uncovered thin sections or grain mounts, finished with 50 nm colloidal alumina. Analytical details (instrument, detector, accelerating voltage, scan rate, gas, and gas pressure) for each image are given in Table 1.

RESULTS

Charge-contrast imaging of cathodoluminescent minerals

Charge trapping in insulators occurs at defects that may correspond to luminescence centers at vacancies, substitution sites, and dislocations in the crystal lattice (Remond et al. 1992). Two cathodoluminescent minerals are considered here—zircon (which shows strong luminescence) and weakly luminescent quartz—to show that CCI can be used to image defects in the same way as CL, and to outline some of the potential advantages of CCI over CL.

Zircon. Zircon ($ZrSiO_4$) is a common accessory mineral in many crustal rocks, and often contains complex internal structures such as concentric euhedral oscillatory growth-zoning, rounded embayments and unconformities due to dissolution or abrasion, multiple stages of crystal growth (magmatic and metamorphic overgrowths and outgrowths on pre-existing grains), recrystallization textures, and grain-scale microfractures when examined in CL (Hanchar and Miller 1993; Pidgeon et al. 1998). Sufficient amounts of U and Pb for isotopic dating are present in zircon, and detailed imaging of internal complexities (using CL, BSE imaging, X-ray mapping, or HF etching coupled with reflected light microscopy) combined with ion microprobe geochronology allows age dating of zones as narrow as 10–20 μm within single crystals. This high spatial resolution allows the discrimination of detrital cores and younger igneous or metamorphic overgrows even in complex, composite zircon crystals containing multiple age domains. Grain maps are produced to facilitate ion beam positioning on the sample, to avoid cracks or the analysis of multiple zones of different ages. The grain map, usually a CL image, is obtained after the epoxy resin grain mount has been gold coated, prior to ion probe analysis. Because the sample surface acts as part of the ion optics of the ion microprobe, great care must be taken to produce and maintain a flat, polished, uniformly conducting sample surface. Zircon crystals are usually small (typically <200 μm), and CL imaging is usually performed at moderate to high magnifications. High magnifications coupled with moderate to high accelerating voltages and high beam currents result in high sample beam dosage and damage to the Au coat and epoxy resin substrate. Thermal damage, ionization and surface contamination by hydrocarbon molecules from the SEM vacuum system may degrade subsequent ion microprobe analyses, and create charging and beam arcing within the ion probe sample chamber.

Figure 4a is a CCI of a zircon from a migmatitic semi-pelite in the Naver Nappe of the Moine Supergroup, NW Scotland. The grain shows a complicated internal architecture consisting of an embayed oscillatory zoned core (interpreted as a refractory detrital zircon that survived a melting event) and a relatively homogeneous rim (which has crystallized from a melt). The two oval features (center and center-left) are analysis pits formed during U–Pb ion microprobe dating of the grain and are less than 1 μm deep. The ion microprobe analysis spot near the center yielded an age of approximately 1250 Ma, whereas the spot on the homogeneous rim gave an age almost 800 My younger (Friend et al. 1999). Two sets of linear features can be recognized running almost horizontally across the upper central part of the grain—a major annealed crack (dark) and a series of smaller bright fractures. Figure 4b is a CL image of the same grain (with an Au coat) taken on a conventional SEM and is almost identical to the CCI image. Both images clearly distinguish a core and a rim, a large rounded embayment (center top), and the ragged annealed fracture (upper center), but

only CCI detected the small bright microfractures. Resolution is at least as good as the CL image because the CCI signal is dominated by SE1 and SE2 electrons (which are generated from a smaller interaction volume than the CL signal), but little difference in the overall zonation pattern can be discerned in the two images.

The striking similarity between CCI and CL images is of interest because the CCI image represents a signal composed of electrons whereas the CL signal is composed of photons. Cathodoluminescence occurs when electron-hole pairs (formed by interaction between the sample and a beam of electrons) recombine and emit radiation over the wavelength range from ultraviolet to near infrared (200–2000 nm). Luminescence centers (sites of photon generation) occur at inhomogeneities and dislocations in the crystal lattice, and may also occur at sites of substitution or insertion of foreign elements (activators). Natural and doped synthetic zircons commonly exhibit strong CL, with several studies noting that CL emission correlates with Dy^{3+} content (summarized in Remond et al. 1992) as part of a coupled $Y–REE^{3+}$ substitution of the form:

$$\left[Zr_{1-e}^{4+}(Y + REE)_{e}^{3+}\right](SiO_4)_{1-x}(OH)_{4x-e}\square_e$$

where □ is a vacancy (i.e., a charge-trapping defect) caused by excess ($Y + REE^{3+}$) ions not compensated by P^{5+} ions replacing Si. Other trivalent REE ions related to CL emission in Zr include Sm, Er, Tb, and Yb (Hanchar and Miller 1993; Remond et al. 1992). Because defects can act to trap charge, CCI provide spatially resolved images of defect concentration the same way that a CL signal does.

Quartz. Figure 5a shows a CCI of a fractured quartz inclusion in garnet from a granulite-facies peraluminous migmatite, and Figure 5b shows the same grain imaged by CL. Both techniques image a network of bright fractures that we interpret as rapidly annealed defect-rich fractures (Watt et al. 2000). Also evident in the CCI image is a broad (20 μm) dark zone around

TABLE 1. ESEM Instrument operating conditions for CCI, BSE, and CL images

Fig.	Instrument	Detector	Accelerating voltage (kV)	Scan rate (ms)	Chamber gas	Gas pressure	Gas pressure	Gas pressure (Pa)
4a	Electroscan E3 ESEM	GSED*	30	60	H_2O	2	266.6	270
4b	JEOL JSM-6400R	CL†	30	120	n/E§	n/E	n/E	n/E
5a	Phillips XL40	GSED	10	120	H_2O	0.1	13.33	10
5b	Phillips XL30	CL	20	120	n/E	n/E	n/E	n/E
6a	Phillips XL40	GSED	30	120	H_2O	0.2	26.66	30
6c	Phillips XL40	BSE	30	120	H_2O	0.2	26.66	30
7a	Phillips XL40	GSED	30	60	H_2O	0.2	26.66	30
7b	Phillips XL40	BSE‡	30	60	H_2O	0.2	26.66	30
7c	Phillips XL40	GSED	30	20 (8 frame average)	H_2O	0.2	26.66	30
9a	Phillips XL40	GSED	30	20 (8 frame average)	H_2O	0.1	13.33	10
9b	Phillips XL40	GSED	30	20 (8 frame average)	H_2O	0.1	13.33	10
9c	Electroscan E3 ESEM	GSED	30	120	H_2O	0.5	66.65	70
10a	Phillips XL40	GSED	25	120	H_2O	0.3	39.99	40
10b	Phillips XL40	GSED	30	120	H_2O	0.2	26.66	30
10c	Phillips XL40	BSE	30	120	H_2O	0.2	26.66	30

* Gaseous secondary electron detector.
† Cathodoluminescence detector.
‡ Backscattered electron detector.
§ Non-ESEM instrument.

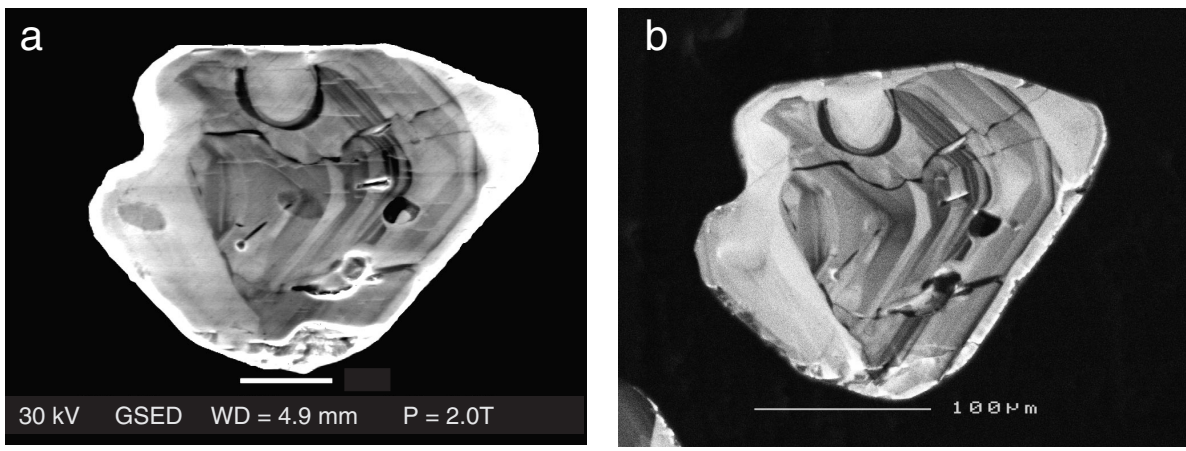

FIGURE 4. (**a**) Charge-contrast and (**b**) cathodoluminescence images of zircon. The CCI image has a slightly higher resolution and detects a series of ca. 20–30 μm bright linear features not visible in CL. Scalebar in a = 50 μm. Imaging conditions for this and all other micrographs are given in Table 1.

a later crack that cuts the bright fracture network. Quartz in granites and migmatites generally shows much weaker luminescence than other luminescent phases such as zircon (D'Lemos et al. 1996; Watt et al. 1997), in part because the structure of quartz only accommodates small amounts of trace element contaminants. Detailed electro-paramagnetic resonance studies coupled with spectral cathodoluminescence have shown that the majority of CL emission from quartz occurs at defects not associated with trace element substitution (Remond et al. 1992; Stevens Kalceff et al. 1999). The principal defects recognized in quartz are E' centers, peroxyl radicals (which consist of an O^{2-} radical bonded to an Si atom bonded to three O atoms), and non-bridging O hole centers (which consist of a hole trapped in a single O atom bonded to a single Si atom bonded to three O atoms) (Stevens Kalceff and Phillips 1995; Stevens Kalceff et al. 1999). All of these defects are capable of trapping charge, and because trapped charge distribution is a direct function of defect concentration (Oh et al. 1993), CCI and CL images of quartz appear similar. One major difference between the two images is the presence of a prominent dark region in CCI. This dark area runs parallel to a late fracture, probably formed during uplift of the migmatite, and is interpreted as a high-conductivity region along which charge is escaping and thus preventing charge-buildup.

Charge-contrast imaging of non-cathodoluminescent minerals

Cathodoluminescence emission only occurs at wide band-gap lattice sites, and therefore only certain minerals exhibit significant luminescence. In contrast, electronic charge can be trapped in many lattice defects and microstructures; therefore, CCI can be completed on almost any mineral phase. To demonstrate the utility of CCI in imaging non-luminescent minerals, we present images of two such phases, biotite and cordierite.

Biotite. Biotite is a trioctahedral sheet silicate consisting of composite $(Si,Al)O_4$ tetrahedral layers linked by octahedrally coordinated cations and additional hydroxyl groups. The composite layers have an overall negative charge and are charge-balanced by a layer of large cations (typically K^+) in 12-fold co-ordination. During metamorphism and deformation, decomposition of (OH) groups and the oxidation of Fe^{2+} encourages the movement of these cations in "cation fluxes" (Guseinov 1999). Vacancy formation during tectonothermal events and consequent ion diffusion may lead to intracrystalline differences in electrical conductivity that can be preserved on cooling (Guseinov 1999). Diffusion in biotites has been the subject of many experimental and theoretical studies involving Ar, because $^{40}Ar/^{39}Ar$ dating of deformed metamorphic rocks often involves the recognition of multiple diffusion pathways (Baldwin et al. 1990; Harrison et al. 1991; Lee 1995; Pickles et al. 1997; Reddy et al. 1997, 1999). Charge-contrast imaging may therefore provide a useful tool for assessing the extent to which microstructures, such as dislocations, deformation bands, subgrain boundaries, or microfractures, can act as short-circuit pathways for rapid diffusion.

Figure 6a shows a CCI of a cluster of biotite grains in a peraluminous granite from East Greenland, with an optical image taken in plane-polarized light (Fig. 6b) and a BSE image (Fig. 6c). Several differences among the images are immediately apparent. Most notable is that CCI picks up fine-scale brightness contrast parallel to the {001} perfect cleavage. Coherent domains within biotite appear to be much narrower (<10 μm) than those evident in the optical and BSE images. It is important to note that the biotite is fresh and unaltered, as evidenced by the absence of chloritic alteration in BSE (Fig. 6c), and that CCI is detecting differences in conductivity within individual biotite crystals rather than compositional contrasts related to alteration. These conductivity contrasts probably reflect differential diffusion domains formed during metamorphism-related dehydroxylation, which can result in clustering of octahedral Fe^{2+} cations and reduced effective diffusion volumes in biotite above 500 °C (Guseinov 1999).

One important feature of Figure 6a is that the pleochroic radiation-damage haloes evident in the optical images of biotite (Fig. 6b) are only weakly detected in CCI. Pleochroic haloes result from lattice damage as a feature of alpha particle emission from minerals containing radioactive isotopes. They are common in biotite due to the presence of zircon and mona-

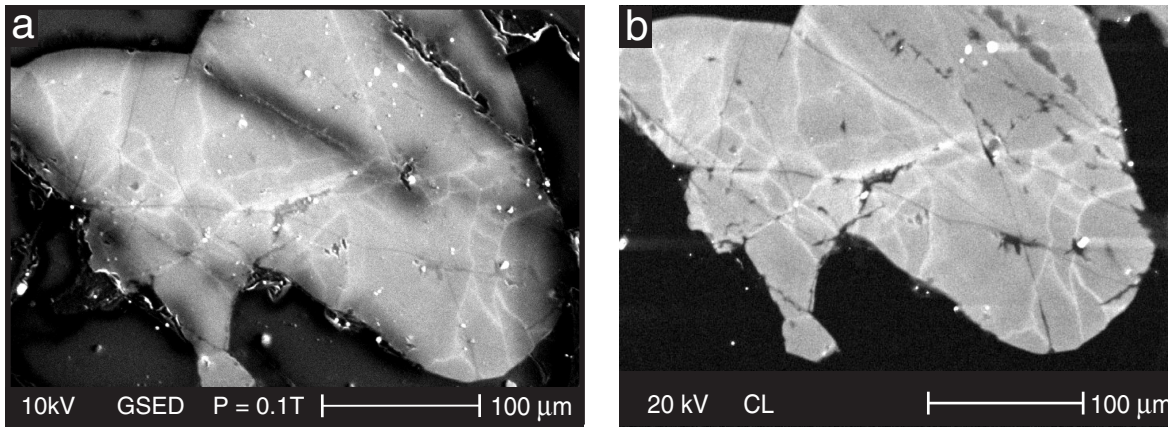

FIGURE 5. (**a**) Charge-contrast and (**b**) cathodoluminescence images of quartz.

zite inclusions, and are important because they may act as fast Ar-diffusion pathways between {001} planes. Because damaged and undamaged lattices should exhibit different charge-trapping behaviors, one might expect to image radiation haloes using CCI and, indeed, Figure 7a shows that it is possible to obtain high-resolution images of radiation haloes. CCI images of radiation-damage haloes have proven to be strongly dependent upon scan rate. Figure 7a was obtained at a scan rate of 60 ms. The bright phases in Figure 7b (a BSE image of the same area) are monazite inclusions that are situated close to grain boundaries. At a scan rate of 60 ms, the haloes (e.g., halo A in Fig. 7a) appear brighter than the surrounding biotite grain. At a faster scan rate (20 ms), the contrast between haloes and undamaged biotite is reversed, and halo B appears darker than the surrounding grain (Fig. 7c). The variations in contrast and the scan-rate dependent reversal of contrast between radiation-damage haloes and undamaged biotite can be explained by considering the relative charging and detrapping rates of the two lattice types, shown schematically in Figure 8. Radiation-damage haloes contain numerous lattice defects and will take longer to reach maximum charge and longer to discharge this charge fully. At slower scan rates (S1, Fig. 8), the halo will retain charge while the undamaged lattice will have experienced almost total detrapping. At faster scan rates, however, charge buildup in the radiation halo is slower, and the undamaged biotite lattice exhibits higher charging. Maximum contrast between halo and lattice will therefore be obtained at particular scan rates (e.g., S2 and S3).

Fracturing, pressure solution, folding, and kinking accompany deformation in biotite, which occurs primarily by slip along {001}. In many cases, these small-scale structures are important in defining diffusion volumes in biotite but are difficult to resolve optically. Figure 9a shows that CCI can be used to image annealed intra-grain fractures in biotite. A conjugate series of fractures approximately 20 μm wide and up to 800 μm long, crosscutting the {001} cleavage at a high angle, can be seen in the central grain. Figures 9b and 9c show a deformed biotite grain from a peraluminous granite. In Figure 9b, the central biotite crystal contains numerous straight fractures, folded cleavage, and small monazite crystals. The fractures are narrow and brighter in CCI than those of Figure 9a, and they show a close spatial association with the monazite inclusions. Monazite grains are also common along grain boundaries in this sample (e.g., Fig 9c). Monazite commonly breaks down during metamorphism (Parnell 1996), releasing Th and REE into metamorphic fluids (Forster and Harlov 1999). Transport of enriched fluids along fractures, cleavage planes, and grain boundaries, and diffusion of fluids into crystals, will alter the conductivity of the host crystals. We suggest that this is a possible explanation for the strong charge contrast evident along the {001} cleavages and fractures in these biotites.

Cordierite. The effects of fluid migration along grain boundaries and intra-grain fractures are clearly demonstrated by cordierite. Cordierite is an Fe-Mg silicate commonly found in metamorphosed pelites and peraluminous granites. Although nominally anhydrous, many naturally occurring cordierites are water bearing. It is readily altered to felted-masses called "pinite," a fine-grained intergrowth of sericite and chlorite.

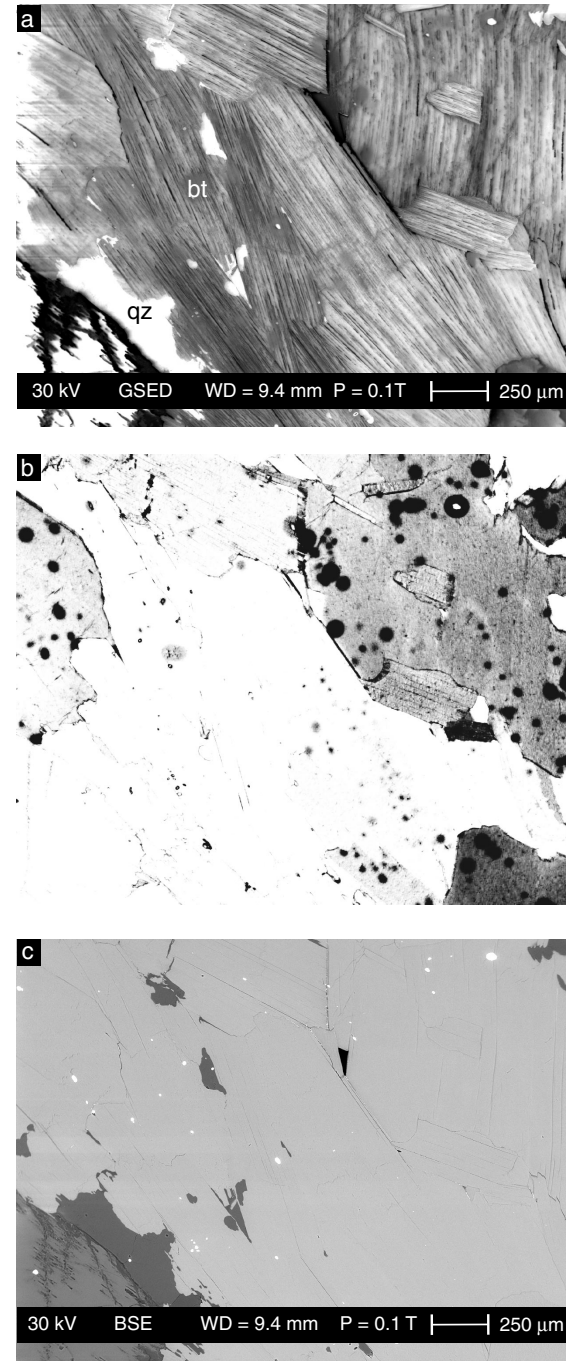

FIGURE 6. (**a**) Charge-contrast image of biotite in a pelitic migmatite. (**b**) Plane-polarized light and (**c**) backscattered electron images of the same area for comparison.

Alteration occurs in the presence of K-rich hydrothermal fluids, which commonly are liberated during the final crystallization stage of granitic melts; thus cordierite in granites is often completely altered. In granulite facies migmatites, however, melts are water-undersaturated and release less H_2O on crystallization; therefore, cordierite in high-grade pelitic migmatites

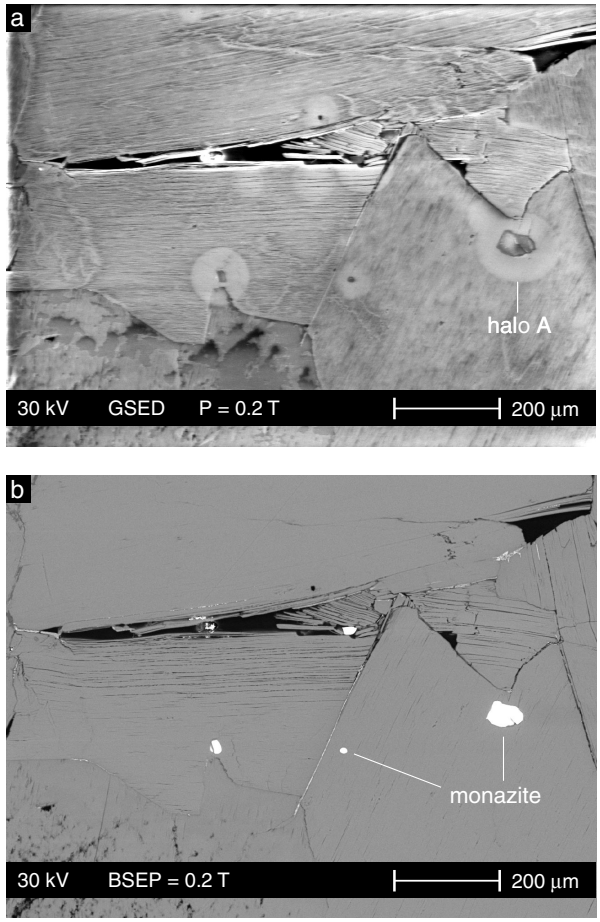

FIGURE 7. (**a**) Charge-contrast image of radiation-damage haloes in biotite in a pelitic migmatite. Note the close spatial association between haloes and grain boundaries. Scan rate = 60 mS. (**b**) Backscattered electron image of the same area, showing monazite crystals (white) that are located in the cores of the haloes. (**c**) 8 frame-averaged, charge-contrast image of the same area taken at a faster scan rate (20 mS). Halo A is now darker than the surrounding biotite grain.

typically shows less alteration. Figure 10a shows a large garnet overgrown by a cordierite-quartz symplectite that formed during decompression of a granulite-facies migmatite. The dark network of veins represents altered cordierite where fluids have passed along fractures and grain boundaries. A detailed view of the altered cordierite (Fig. 10b) shows that the extent of this alteration appears much greater in CCI than in a BSE image of the same area (Fig. 10c). Fluids have altered the cordierite structure around the margins of the vein network, giving rise to broad zones of dark charge contrast. Other phases in the rock, including garnet and quartz, have experienced less alteration, but biotite at the edge of the cordierite crystal has clearly been affected by late-stage fluid circulation along {001} cleavage planes (Fig. 10a).

SUMMARY

We have demonstrated that charge-contrast imaging can be used to obtain high-resolution topographic, structural, and compositional information from differences in charging and charge detrapping (e.g., conductivity) in minerals of geological interest. The charge-contrast signal is composed of a cascade of electrons produced by gas amplification in the chamber of an environmental scanning electron microscope. Gas pressure and electron beam dosage are balanced so that a small amount of charge is implanted into the sample. Secondary electron emission, enhanced by charging and suppressed by the positive ion flood, varies according to conductivity and allows the direct imaging of intra- and inter-grain conductivity contrasts.

Imaging of cathodoluminescent minerals shows that the processes controlling CCI and CL are very similar. Contrast in the CCI image is related to charge-controlled, enhanced or suppressed electron emission, whereas the CL signal results from

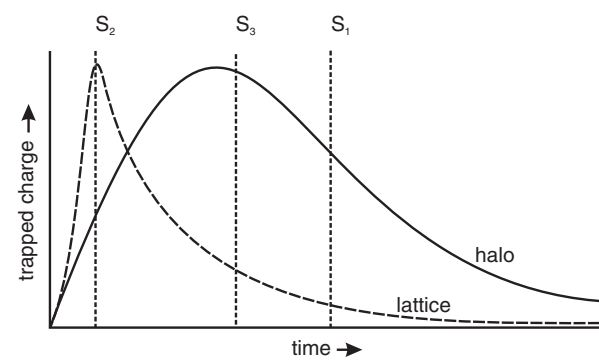

FIGURE 8. Schematic plot showing the effect of scan rate on relative contrast between a rapid charge trapping/detrapping site (e.g., biotite lattice) and a site with a slower charge-trapping time constant (e.g., radiation-damaged haloes around monazite). At scan rate S1, the halo will contain more trapped charge than the undamaged lattice and will thus appear brighter than the surrounding biotite (e.g., Fig. 7a). At faster scan rates (e.g., S2), charge buildup in the lattice is greater than that in the halo, producing contrast reversal compared with S1. Contrast maxima will occur at scan rates S2 and S3.

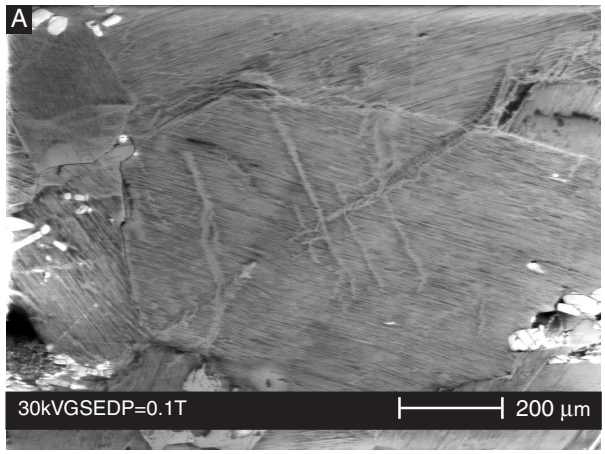

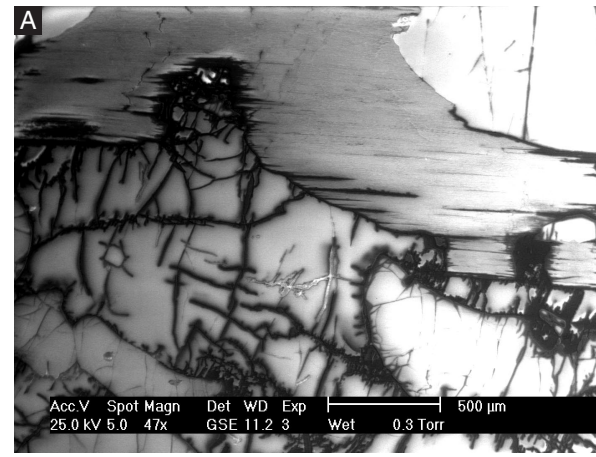

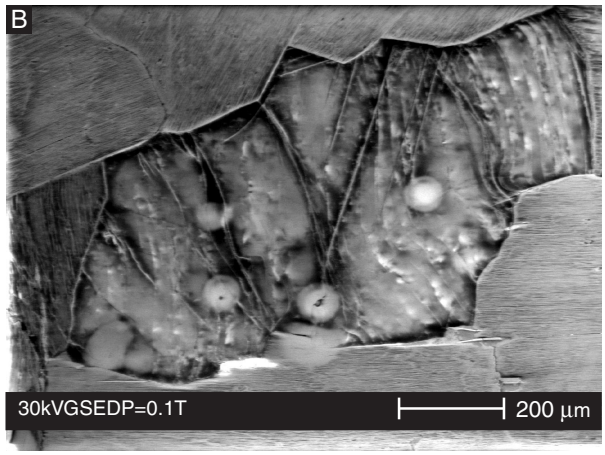

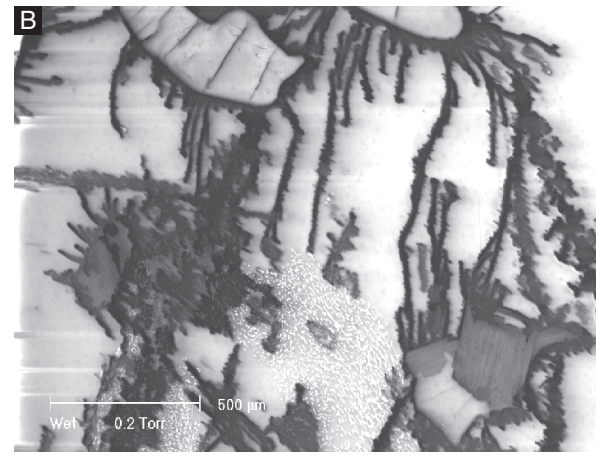

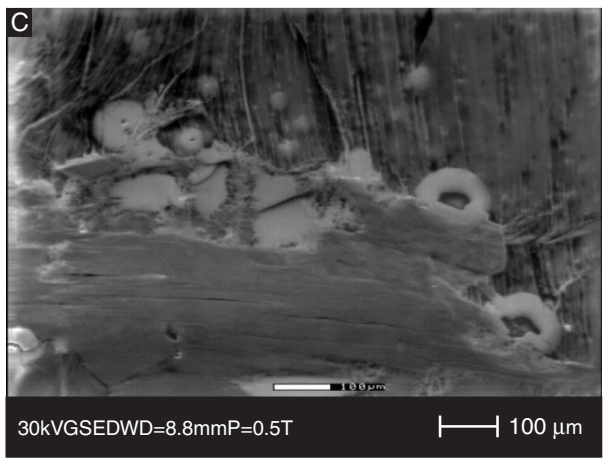

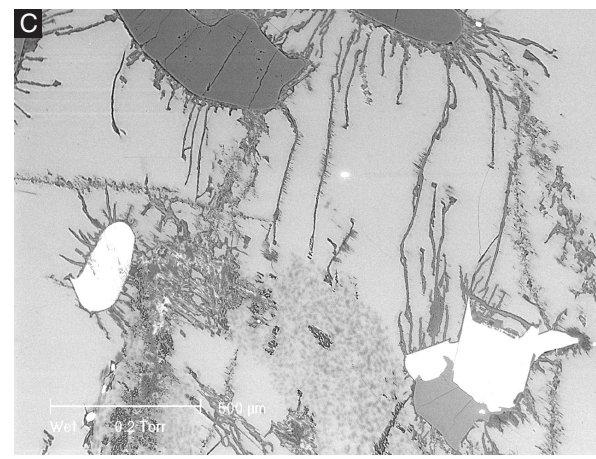

FIGURE 9. (**A**) Charge-contrast image of cross-cutting annealed fractures in biotite. (**B**) Charge-contrast image of fractures in biotite containing <10 µm monazites and associated radiation damage haloes. (**C**) Charge contrast image of biotite showing location of monazite inclusions along grain boundaries.

FIGURE 10. (**A**) Charge-contrast image of alteration in cordierite and biotite. (**B**) Charge-contrast and (**C**) Backscattered electron images of altered cordierite. CCI clearly shows that fluid-related alteration is much more pervasive than indicated in the backscattered electron image.

photon emission due to de-excitation at defect centers. Strongly luminescent minerals such as zircon, which contain abundant defects related to the substitution of trace elements and consequent lattice distortions, and more weakly luminescent minerals (e.g., quartz from granitic igneous rocks) can be imaged with CCI.

Because electronic charge can be trapped at lattice sites and defects that do not have a suitable band gap to generate CL, CCI also can be used as a high-resolution imaging method in non-luminescent minerals as well. In our examples, microstructures such as fractures and kink bands are clearly discernible in CCI. Fluid-flow pathways and their controls on the redistribution of soluble accessory phases such as monazite are also readily seen. Fluid flow plays a major role in many crustal processes including large-scale mass and heat transfer during metamorphism (Ague 1994; Gerdes and Valley 1990; Hoisch 1991), isotopic resetting (Cartwright and Buick 1998; Graham et al. 1998), the location of ore deposits (Cathles 1981), and the creation or destruction of porosity by fluid flow in sandstone reservoirs (Marret and Laubach 1997). Whereas calculations of fluid fluxes (Bickle and Baker 1990; Dipple and Ferry 1992) and the identification of kilometer-scale structural pathways (Skelton 1996) enable us to model large-scale crustal fluid pathways (at scales ranging from 100 km to 1 cm), the mechanisms that control grain-scale fluid movements are comparatively poorly understood. We therefore suggest that one of the most exciting future applications of charge-contrast imaging may be in direct imaging of relict fluid pathways in rocks that have experienced metasomatism or alteration.

ACKNOWLEDGMENTS

This study was supported by an ARC Small Grant to Watt. Reviews by L.M. Wang, Donggao Zhao, and Rod Ewing greatly improved the manuscript. We thank James Browne and Roz Wealthall for help with charge contrast and cathodoluminescence imaging, Peter Glover for sample preparation and Steve Reddy, Peter Cawood, and Simon Bodorkos for early reviews and informative and thought-provoking discussions. This is Tectonics Special Research Centre Publication Number 107.

REFERENCES CITED

Ague, J.J. (1994) Mass transfer during Barrovian metamorphism of pelites, south-central Connecticut, II. Channelized fluid flow and the growth of staurolite and kyanite. American Journal of Science, 294, 1061–1134.

Baldwin, S.L., Harrison, T.M., and Fitz Gerald, J.D. (1990) Diffusion of ^{40}Ar in metamorphic hornblende. Contributions to Mineralogy and Petrology, 105, 691–703.

Baroni, T., Griffin, B.J., and Lincoln, F.J. (1999) Applying electron probe techniques to understand crystallisation processes in gibbsite. Proceedings of the 1999 Joint WASEM/AXAA(WA) 1999 Joint Conference, 20–22.

Bickle, M.J. and Baker, J. (1990) Advective-diffusive transport of isotopic fronts: an example from Naxos, Greece. Earth and Planetary Science Letters, 97, 78–93.

Cartwright, I. and Buick, I.S. (1998) The link between oxygen isotope resetting, partial melting and fluid flow in metamorphic terrains. Terra Nova, 10, 81–85.

Cathles, L.M. (1981) Fluid flow and genesis of ore deposits. Economic Geology, 75th Anniversary Volume, 424–457.

Danilatos, G.D. (1993) Introduction to the ESEM instrument. Microscopy Research and Technique, 25, 354–361.

Dipple, G.M. and Ferry, J.M. (1992) Metasomatism and fluid flow in ductile fault zones. Contributions to Mineralogy and Petrology, 112, 149–164.

D'Lemos, R.S., Kearsley, A.T., Pembroke, J.W., Watt, G.R., and Wright, P. (1996) Quartz growth histories in granite revealed by scanning cathodoluminescence techniques. Geological Magazine, 134, 549–552.

Doehne, E. (1998) Charge contrast: some ESEM observations of a new/old phenomena. In G.W. Bailey, Ed. Microscopy and Microanalysis 1997, 4 (Supplement 2), p. 292–293. Springer, Atlanta, Georgia.

Forster, H.J. and Harlov, D.E. (1999) Monazite-(Ce)-huttonite solid solutions in granulite-facies metabasites from the Ivrea-verbano Zone, Italy. Mineralogical Magazine, 63, 587–594.

Friend, C.R.L., Kinny, P.D., Strachan, R.A., Watt, G.R., and Burns, I.M. (1999) U–Pb Geochronology and tectonothermal evolution of Caledonian migmatites, East Sutherland, Scotland. Journal of the Geological Society of London, 156, 1143–1152.

Galvin, S.P. and Griffin, B.J. (1999) Application of charge contrast imaging to the study of densified regions in fused silica and to the study of glass polishing. Proceedings of the 1999 Joint WASEM and AXAA(WA) State Conference, 57–58.

Gerdes, M.L. and Valley, J.W. (1990) Fluid-rock interaction at the Valentine Wollastonite Mine, NW Adirondack mountains, N.Y.: Multiple episodes of channelized fluid infiltration. Geological Society of America abstracts with programs, 22(7), 212.

Gluszak, E.A., Hinckley, S., Griffin, B.J., Redfern, D., Musca, C.A., and Faraone, L. (1999) Charge contrast imaging of SWIR and MWIR HgCdTe photodiodes. Proceedings of the 1999 Joint WASEM/AXAA(WA) 1999 Joint Conference, 64–65.

Gong, H., Le Gressus, C., Oh, K.H., Ding, X.H., Ong, C.K., and Tan, B.T.G. (1993) Charge trapping on different cuts of a single-crystalline a–SiO_2. Journal of Applied Physics, 74, 1944–1948.

Graham, C.M., Valley, J.W., Eiler, J.M., and Wada, H. (1998) Timescales and mechanisms of fluid infiltration in a marble: an ion microprobe study. Contributions to Mineralogy and Petrology, 132, 371–389.

Griffin, B.J. (1997) A new mechanism for the imaging of crystal structure in non-conductive materials: an application of charge-contrast in the environmental scanning electron microscope (ESEM). In G.W. Bailey, R.V.W. Dimlich, K.B. Alexander, J.J. McCarthy, and T.P. Pretlow, Eds. Microscopy and Microanalysis 1997, 3 (Supplement 2), p. 1197–1198. Springer, Cleveland, Ohio.

———(1998) Electrons, ions and cathodoluminescence in the environmental SEM. In G.W. Bailey, Ed. Microscopy and Microanalysis 1997, 4 (Supplement 2), p. 290–291. Springer, Atlanta, Georgia.

Griscom, D.L. (1990) Electron spin resonance investigations of defects and defect processes in amorphous silicon dioxide. Reviews of Solid State Science, 4, 565–599.

Guseinov, A.A. (1999) Relationship between ion conductivity and the heat-induced processes of oxidation and dehydroxylation in ferrous-magnesian micas. Geochemistry International, 37, 87–90.

Hanchar, J.M. and Miller, C.F. (1993) Zircon zonation patterns as revealed by cathodoluminescence and backscattered electron images: Implications for interpretation of complex crustal histories. Chemical Geology, 110, 1–13.

Harker, A.B., DeNatale, F.F., Flintoff, J.F., and Breen, J.J. (1993) Direct observation of the defect structure of polycrystalline diamond by scanning electron microscopy. Applied Physics Letters, 62, 105–107.

Harker, A.B., Howitt, D.G., DeNatale, J.F., and Flintoff, J.F. (1994) Charge-sensitive secondary electron imaging of diamond microstructures. Scanning, 16, 87–90.

Harrison, T.M., Lovera, O.M., and Heizler, M.T. (1991) ^{40}Ar/^{39}Ar results for alkali feldspars containing diffusion domains with differing activation-energy. Geochimica et Cosmochimica Acta, 55, 1435–1448.

Hoisch, T.D. (1991) The thermal effects of pervasive and channelized fluid flow in the deep crust. Journal of Geology, 99, 69–80.

Kronenberg, A.K. and Kirby, S.H. (1987) Ionic conductivity of quartz: DC time dependence and transition in charge carriers. American Mineralogist, 72, 739–747.

Lee, J.K.W. (1995) Multipath diffusion in geochronology. Contributions to Mineralogy and Petrology, 120, 60–82.

Lloyd, G.E. and Hall, M.G. (1981) Applications of scanning electron microscopy to the study of deformed rocks. Tectonophysics, 78, 687–698.

Marret, R. and Laubach, S.E. (1997) Diagenetic controls on fracture permeability and sealing. Journal of Rock Mechanics and Mineral Science, 34, 409.

Meredith, P., Donald, A.M., and Thiel, B. (1996) Electron-gas interactions in the environmental scanning electron microscopes gaseous detector. Scanning, 18, 467–473.

Newton-Howes, J.C., McLaren, A.C., and Fleming, R.J. (1989) An investigation of the effects of hydroxyl concentration and bubble formation on the electrical conductivity of synthetic quartz. Tectonophysics, 158, 335–342.

Oh, K.H., Ong, C.K., Tan, B.T.G., and Le Gressus, G. (1993) A Monte Carlo model for trapped charge distribution in electron-irradiated a–quartz. Journal of Applied Physics, 74, 6859–6865.

Parnell, J. (1996) Alteration of crystalline basement rocks by hydrocarbon-bearing fluids: Moinian of Ross-shire, Scotland. Lithos, 37, 281–292.

Pickles, C.S., Kelley, S.P., Reddy, S.M., and Wheeler, J. (1997) Determinations of high spatial resolution argon isotope variations in metamorphic biotites. Geochimica Cosmochimica Acta, 61, 3809–3824.

Pidgeon, R.T., Nemchin, A.A., and Hitchen, G.J. (1998) Internal structures of zircons from Archaean granites from the Darling Range batholith: implications for zircon stability and the interpretation of zircon U–Pb ages. Contributions to

Mineralogy and Petrology, 132, 288–299.
Reddy, S.M., Kelley, S.P., and Magennis, L. (1997) A microstructural and argon laserprobe study of shear zone development on the western margin of the Nanga Parbat Syntaxis, north Pakistan. Contributions to Mineralogy and Petrology, 128, 16–29.
Reddy, S.M., Potts, G.J., Kelley, S.P., and Arnaud, N.O. (1999) The effects of deformation-induced microstructures on intragrain $^{40}Ar/^{39}Ar$ ages in potassium feldspar. Geology, 27, 363–366.
Reimer, L. (1985) Scanning Electron Microscopy: Physics of Image Formation and Microanalysis. 457 p. Springer-Verlag, Berlin.
Remond, G., Cesbron, F., Chapoulie, R., Ohnenstetter, D., Roques-Carmes, C., and Schvoerer, M. (1992) Cathodoluminescence applied to the microcharacterisation of mineral materials; a present status in experimentation and interpretation. Scanning Microscopy, 6, 23–68.
Sawyer, G.R. and Page, T.F. (1978) Microstructural characterisation of "REFEL" reaction bonded silicon carbide. Journal of Materials Science, 13, 885–904.
Siegel, G.H. and Marrone, M.J. (1981) Photoluminescence in as-drawn and irradiated silica optical fibres: an assessment of the role of non-bridging oxygen defect centres. Journal of Non-Crystalline Solids, 13, 372–398.
Skelton, A.D.L. (1996) The timing and direction of metamorphic fluid flow in Vermont. Contributions to Mineralogy and Petrology, 125, 75–84.
Stevens Kalceff, M.A. and Phillips, M.R. (1995) Cathodoluminescence microcharacterization of the defect structure of quartz. Physical Review B, 52, 3122–3134.
Stevens Kalceff, M.A., Thorogood, G.J., and Short, K.T. (1999) Charge trapping and defect segregation in quartz. Journal of Applied Physics, 86, 205–208.
Thiel, B.L., Fletcher, A.L., and Donald, A.M. (1997) Comparison of amplification and imaging behaviours of several gases in the environmental SEM. In G.W. Bailey, R.V.W. Dimlich, K.B. Alexander, J.J. McCarthy, and T.P. Pretlow, Eds. Microscopy and Microanalysis 1997, 3 (Supplement 2), p. 1195–1196. Springer, Cleveland, Ohio.
Thumm, U., Ducrée, J., Kürpick, P., and Wille, U. (1999) Charge transfer and electron emission in ion-surface interactions. Nuclear Instruments and Methods in Physics Research (B): Beam interactions with materials and atoms, 157, 11–20.
Trimby, P.W. and Prior, D.J. (1999) Microstructural imaging techniques: a comparison between light and scanning electron microscopy. Tectonophysics, 303, 71–81.
Vigouroux, J.P., Duraud, J.P., Le Moel, A., and Le Gressus, C. (1985) Electron trapping in amorphous SiO_2 studied by charge buildup under electron bombardment. Journal of Applied Physics, 57, 5139–5144.
Watt, G.R., Wright, P., Galloway, S., and McLean, C. (1997) Cathodoluminescence and trace element zoning in quartz phenocrysts and xenocrysts. Geochimica Cosmochimica Acta, 61, 4337–4348.
Watt, G.R., Oliver, N.H.S. and Griffin, B.J. (2000) Evidence for reaction-induced microfracturing in granulite-facies migmatites. Geology, 28, 327–330.

MANUSCRIPT RECEIVED JANUARY 4, 2000
MANUSCRIPT ACCEPTED JULY 7, 2000
PAPER HANDLED BY RODNEY C. EWING